MEGAPIXEL IMAGE GENERATION WITH STEP-UNROLLED DENOISING AUTOENCODERS

Alex F. McKinney & Chris G. Willcocks
Department of Computer Science
Durham University
Durham, UK
{alexander.f.mckinney,christopher.g.willcocks}@durham.ac.uk

ABSTRACT

One recent trend in generative modelling research has been to push sample resolutions higher whilst simultaneously reducing computational requirements for training and sampling. We aim to push this trend further via the combination of various recent advancements across deep learning – each component representing the pinnacle of efficiency in their respective areas. These include vector-quantized GAN (VQ-GAN), a vector-quantization (VQ) model capable of high levels of lossy – but perceptually insignificant – compression; hourglass transformers, a highly scaleable self-attention model; and step-unrolled denoising autoencoders (SUNDAE), a non-autoregressive (NAR) text generative model. Unexpectedly, our method highlights weaknesses in the original formulation of hourglass transformers when applied to multi-dimensional data. In light of this, we propose multiple modifications to their architecture, with ramifications in the wider field of multi-dimensional data modelling using hierarchical transformers. The combination of these techniques results in a highly efficient generative model framework, both in terms of scalability and sampling speed of our model. Our proposed framework scales to high-resolutions (1024×1024) easily, and can be trained quickly (4-6 days). Crucially, the trained model produces diverse and realistic megapixel samples in approximately 2 seconds. This is considerably faster sampling (minutes, or even tens of minutes) and training ($>$ 10 days) than existing non-adversarial methods at this resolution. In general, the framework is flexible: supporting an arbitrary number of sampling steps, sample-wise self-stopping, self-correction capabilities, conditional generation, and a NAR formulation that allows for arbitrary inpainting masks.

Figure 1: High-resolution samples produced using our non-autoregressive approach. Each 1024×1024 sample was generated in $\approx$ 2 seconds on a GTX 1080Ti – including both discrete latent sampling and subsequent VQ-GAN decoding. At this resolution, autoregressive and (non-adversarial) non-autoregressive models take minutes to sample, or simply do not scale to this resolution. Training is similarly fast, with the FFHQ1024 model taking 4 days to train on a single Nvidia V100 32GiB.

1 INTRODUCTION

An ideal deep generative model satisfies three key requirements: high-quality samples, mode coverage resulting in high sample diversity, and computationally inexpensive sampling. Arguably, there are other desirable properties such as a meaningful latent space, exact likelihood calculation, and controlled generation. Nonetheless, no current generative model satisfies all three key requirements – let alone additional attractive properties – forming the so-called generative modelling trilemma [58] that dominates modern generative modelling research.

Models such as generative adversarial networks (GANs) [20] excel at high-quality and fast sampling, but often fail to model the entire data distribution and are notoriously unstable due to not directly optimising for likelihood, using an adversarial loss as a proxy. Variational auto-encoders (VAEs) [30] offer excellent mode coverage and fast sampling speeds, but the resulting samples are blurry even at small resolutions, and cannot meaningfully scale to the high resolutions obtained by GANs.

Autoregressive (AR) models such as PixelSnail [6], Image Transformer [37], and DALL·E [37] have demonstrated respectable sample quality and mode coverage, even extending to zero-shot image generation [40]. However, they are computationally expensive to sample from, requiring many network iterations to produce a single sample, with the number of iterations scaling linearly with data dimensionality. This makes them infeasible for use in interactive applications. Denoising diffusion probabilistic models (DDPMs) [22] and score-based models (SBMs) [46, 47, 48] produce samples that rival or exceed the quality of GANs [14] whilst providing excellent mode coverage, but are plagued still by potentially requiring thousands of network evaluations per sample.

VQ image modelling [54, 41, 18] alleviates sampling speed issues in AR methods by reducing the spatial dimension at which discrete AR priors operate. This results in excellent quality samples whilst improving sampling speeds, but mandates a two-stage training approach and is still slower than GANs. Recent work has applied diffusion models to VQ latents [3] allowing for fast parallel sampling. Concurrent work used continuous latent spaces to accelerate sampling [58, 51].

This overview of generative modelling demonstrates that no approach satisfies all three requirements. This motivates research into explicitly addressing this trilemma. In this work, we move towards such a solution, beginning from existing work applying generative models to discrete latents. This provides an excellent starting point in terms of sample quality and mode coverage, but slow sampling speeds despite the reduced spatial dimension of the discrete latent space. We address this issue by sampling latents using a non-autoregressive (NAR) generative model to close the gap, sampling speed wise, with models such as GANs. Specifically, we use discrete step-unrolled denoising autoencoders (SUNDAE) [44] to denoise samples from a uniform prior into samples from the discrete latent space defined by a trained vector-quantized GAN (VQ-GAN) model. We find that SUNDAE is an effective discrete prior over VQ-GAN representations.

SUNDAE has only previously be applied to language modelling tasks [44] using transformer [56] architectures in their autoencoder. Parallel work introduced a drastically more efficient variant – the hourglass transformer [36] – leveraging a hierarchical architecture targeting language modelling. Though able to be applied to discrete latent modelling, we propose a number of improvements that improve performance on multi-dimensional discrete data, including modifications to resampling operations and introduction of axial positional embeddings [49]. Though evaluated on discrete latents, these modifications are applicable to any multi-dimensional data, which is valuable in a wider context outside generative modelling. We also found recommended parameters proposed in Savinov et al. [44] did not always generalise to multi-dimensional data, so we explore new sensible defaults in this work.

Given a fast sampling and efficient transformer architecture, we now possess a highly scaleable generative model, with respect to number of layers and spatial resolution of the latent input. Only a minority of the layers are operating at the same resolution as the input, reducing the impact of costly self-attention. Conversely, we cheaply scale the number of layers by adding layers only at the downsampled resolution, allowing for considerably larger models with minor additional cost. To demonstrate this scalability, we train a VQ-GAN operating on 1024×1024 images and apply our framework to the resulting discrete latents. This results in the synthesis of megapixel images in as few as two seconds on a consumer-grade GPU. To our knowledge, this is the largest VQ-GAN trained in terms of input size, and the fastest sampling non-adversarial generative framework at this image resolution.

Our contributions as a result of this research project are as follows:

- The development of a non-autoregressive, non-adversarial generative modelling framework with extremely flexible sampling including self-correction, sample-wise self-stopping, conditional generation, and arbitrary inpainting pattern capabilities. The model can be directly configured for both low- and high-step sampling scenarios, capable of high quality and diverse samples in mere seconds of sampling time.
- Modifications to methods proposed in Savinov et al. [44] and Nawrot et al. [36] to be more suited for the modelling of multi-dimensional discrete data. Though applied to discrete latents in our work, the modifications are applicable in a wider context, such as to pixel-level modelling. We also demonstrate the superiority of hierarchical transformers – a crucial component in the scalability of our approach.
- The scaling of VQ-GAN [18] to extremely high resolution images of human faces. 1024×1024 images far exceeds the resolution of prior work using VQ-GAN. This allowed for the **generation of megapixel images in as few as two seconds** on a consumer-grade GPU when combined with our trained discrete prior

SUNDAE. In contrast, prior AR methods and non-adversarial NAR methods take minutes to sample, or have not been scaled to such resolutions.

2 Related Work

This work builds upon much prior research into powerful deep generative models, self-supervised representation methods, and efficient transformer architectures. We cover relevant work into deep generative models in §2.1 and §2.2, vector-quantized image modelling in §2.3, a specific NAR generative model SUNDAE in §2.4, and an efficient transformer architecture in §2.5. For a full review on generative modelling we direct the reader to Bond-Taylor et al. [4], and on SUNDAE and hourglass transformers to Savinov et al. [44] and Nawrot et al. [36] respectively.

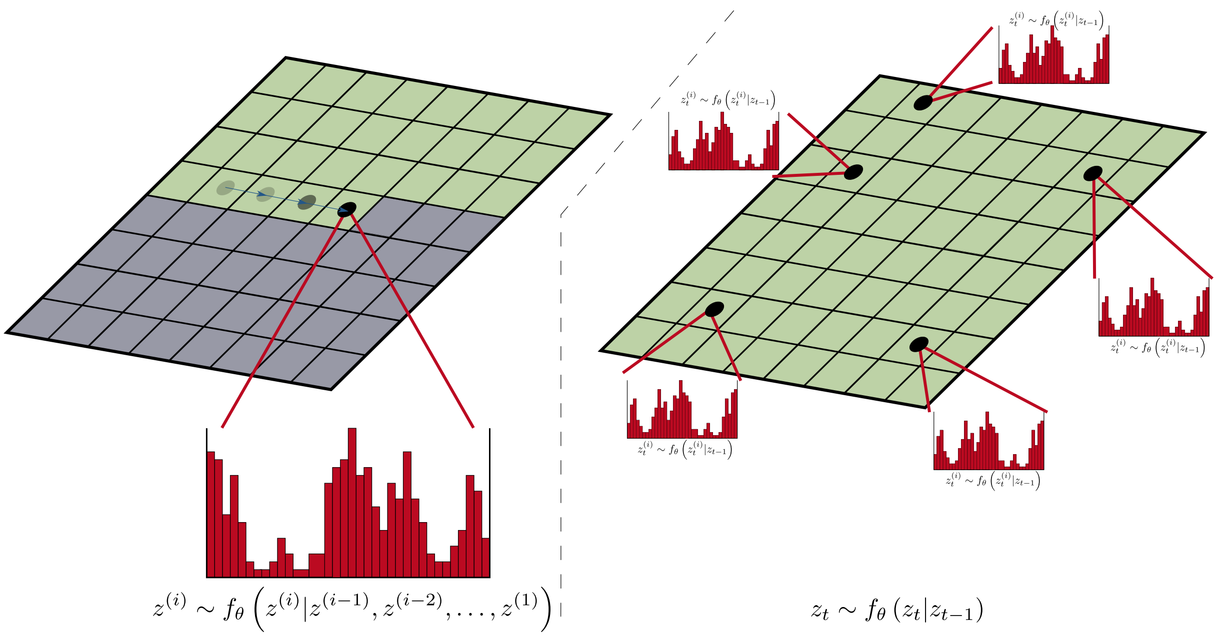

Figure 2: **Left:** Visualization of autoregressive (AR) sampling. AR sampling proceeds one element at a time, meaning the number of sampling steps is equal to the dimensionality of the input. For each element, a probability distribution over possible discrete values is predicted and subsequently sampled from. Each prediction can only make use of past context – indicated as a green position – so not to violate the autoregressive property. **Right:** Visualization of non-autoregressive (NAR) sampling. NAR sampling samples an arbitrary number of elements in parallel, including elements previously sampled, allowing for self-correction. It freely uses all context available, allowing for flexible inpainting and better predictions.

2.1 Autoregressive Generative Models

One major deep generative model family are autoregressive (AR) models, characterised by a training and inference process based on the probabilistic chain rule. During training, they learn to maximise the likelihood of the data they are trained on, which leads to excellent mode coverage. Prior work using these methods resulted in impressive results in terms of sample quality and diversity, but are ultimately impractical in most real world applications due to their slow sampling speed.

The slow speed is due to their sequential nature, defined by the chain rule of probability. Given an input $\mathbf{x} = \{x_1, x_2, \ldots, x_n\}$, an AR model $p_\theta(\cdot)$ generates new samples sequentially:

$$p_\theta(\mathbf{x}) = p_\theta(x_1, \ldots, x_n) = \prod_{i=1}^{n} p_\theta(x_i | x_1, \ldots, x_{i-1}) \tag{1}$$

meaning that the number of sampling steps is equal to the size of the decomposition of $\mathbf{x}$, giving an iteration complexity of $\mathcal{O}(n)$.

For certain tasks, the ordering of the decomposition of $\mathbf{x}$ is obvious, for example on text or speech. For images this is less clear, but typically a raster scan ordering is used [37]. Certain AR models are order-agnostic [24], allowing for arbitrary ordering to be used during training and inference.

One class of AR models are recurrent neural networks (RNNs) which are an early example of using neural networks to model sequential data such as text, audio, time-series data, or even handwriting strokes. Though they can be used as classification or regression models, they are also suited for use as generative models by modelling the relationship in Equation 1. They suffer from a number of issues, most infamously vanishing gradients [38] and inability to model long-range relationships between elements in the input. Long short-term memory recurrent neural networks (LSTMs) [23] improved upon RNNs by introducing dedicated memory units, allowing for the modelling of long-range relationships. Gated recurrent units (GRUs) [9] simplified the LSTM architecture whilst retaining good performance. With the advent of transformer architectures [56], modelling longer relationships became possible, even at a full-document level. It also introduced the capability to train on all sequence elements in parallel through the use of causal masking, therefore not violating the autoregressive property. Inference must still be done in a sequential manner, however.

Applying AR models to images followed a similar progression. PixelRNN [52] used two-dimensional recurrent layers and residual connections to model the distribution of raw pixel values. The same paper also introduced PixelCNN, which had worse performance but is faster to train. These were extended to allow for conditional generation in [53]. Later work augmented PixelCNN with self-attention mechanism, forming PixelSnail [6], which can model longer relationships than a fully convolutional or recurrent architecture. Image Transformer [37] later applied transformer architectures to the same task through an effective but conceptually simple approach. In all cases, the iteration complexity is still $\mathcal{O}(n)$, a property intrinsic to AR models.

2.2 Non-autoregressive Generative Models

Non-autoregressive (NAR) generative models include GANs, SBMs and DDPMs, and flow-based models. The number of sampling steps in NAR models is independent of the data dimensionality, however the actual number of steps varies greatly: from single-step generation in GANs to many thousands in early diffusion models.

The most infamous class of NAR generative model – or generative model altogether – are generative adversarial networks (GANs) [20]. GANs consist of two components: a generator that creates samples from latent variables, and a discriminator that attempts to distinguish samples from the dataset from samples from the generator [20]. They are known for high-fidelity samples, fast sampling, unstable training, and tendency to collapse onto a subset of modes of the data distribution, due to not optimising directly for likelihood. This is reflected in its relatively low-diversity samples. Nonetheless, the quality and speed of the samples have made them a popular choice in a variety of applications, including unconditional and conditional generation [27, 5], image and audio synthesis [33], and style transfer [62]. They can be applied to discrete data [12], but are less effective due to the non-differentiability of discrete samples.

Variational auto-encoders (VAEs) [30] are a class of generative model which permit sampling in a single forward pass like GANs, but are trained to maximise likelihood. Specifically, VAEs map inputs to latent variables that follow some easy to sample, but sufficiently complex, prior distribution. A common choice is a multivariate Gaussian with diagonal covariance [30]. A decoder network maps latent codes to the data distribution. Although this approach is successful on simple datasets, on complex datasets the samples and reconstructions become blurry, suggesting a simple prior is insufficient to model the data distribution. Later work extended VAEs to be hierarchical, having multiple Gaussian priors [50, 7], which was found to outperform AR models.

Another non-adversarial NAR class that permits sampling in a single forward pass are normalizing flows, a class of generative model that allows for exact likelihood calculation [15, 16, 31]. They consist of many invertible layers that transform samples from a known prior distribution into samples from the data distribution. Each transformation must satisfy two properties: being invertible and having an easy to compute Jacobian for scaling [15, 16]. This means the architectural choices are restricted, making them parameter inefficient. They also must operate at the same dimensionality for each layer, making the training of deep networks difficult.

Denoising diffusion probabilistic models (DDPMs) [22, 14] and score-based models (SBMs) [46, 47, 48, 51] have garnered much interest in recent work, with the former learning to estimate the noise and the latter trained to remove noise, given samples from a corrupting forward process. Either method can then be used to move from noise to data, forming a generative model [46]. Both are slow to sample from, but produce high quality samples that rival those of GANs [14] whilst not suffering from mode collapse. The slow sampling speed can be remedied using a variety of techniques, such as operating over a smaller latent space [51], devising efficient SDE solvers [26], or by diffusing "velocities", thus simplifying the denoising task [17]. Unlike GANs, both models can operate on discrete data, either by projecting discrete data into a continuous latent space [51] or with a discrete diffusion framework [1], the latter of which bridges the gap between diffusion, autoregressive, and mask-based representation models such as BERT [13]. Despite the iteration complexity no longer being $\mathcal{O}(n)$, there is a still a gap between the sampling speed of adversarial and non-adversarial methods.

2.3 Vector Quantized Image Modelling

Learning useful latent representations, also known as latent codes, in an unsupervised manner is a key challenge in machine learning. Historically, these representations have been continuous, but in recent work they are often discrete. An early example is vector-quantized VAE (VQ-VAE) [54], which has three main components: an encoder network, a codebook, and a decoder. The encoder network outputs a compressed continuous representation of the input, and the codebook $\mathcal{C}$ quantizes these representations, outputting discrete indices from 1 to the codebook size v. Each index i maps to one of the codebook embeddings (codewords) e_i. The decoder maps the quantized embeddings to a lossy reconstruction of the input. VQ-VAE is trained end-to-end to reconstruct the input and to minimize the codebook loss [54]. Once trained, an auxiliary generative model is trained to generate the discrete latent representations. The decoder then decodes the sampled latent, producing the final sample. In the original work, PixelCNN was used to generate the discrete latent codes [54], though any generative model for discrete data can be used.

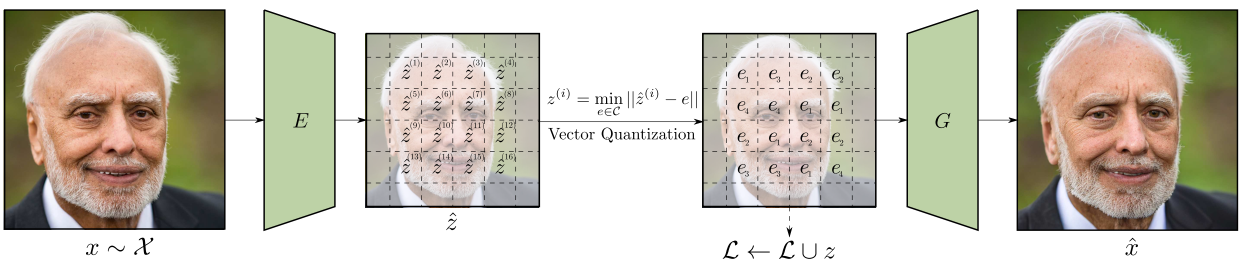

Figure 3: Visualisation of a vector-quantization image model. An encoder model extracts continuous representations from the input. Vector quantization is then used to map each continuous embedding to the closest entry in the codebook. A decoder model takes the discretized embeddings outputs a lossy reconstruction of the input. We generate a dataset of latent representations from an image dataset by iterating $\mathbf{x} \in \mathcal{X}$ and appending the resulting discrete representation $\mathbf{z}$ to a set $\mathcal{L}$.

Later approaches extended VQ-VAE to multiple hierarchical codebooks in VQ-VAE-2 [41]. Though it can be extended to any number of codebooks, they experimented with at most three, applying it to 1024×1024 images. They then sampled the hierarchical discrete representations using multiple PixelSnail [6] models, each code conditioned on all previous levels in the hierarchy. Though faster to sample than generating pixels directly, at such a resolution and with multiple representation levels, sampling times were still very slow.

Aside from sampling autoregressively, a reason for the slow sampling speed is the large spatial resolution of the discrete codes. Albeit smaller than the original input, VQ-VAE is limited in how much it can compress the signal via a simple reconstruction objective before it loses significant perceptual quality, due to the rate-distortion trade-off. For example, the original VQ-VAE only has a downsampling rate of $f = 4$ [54] and VQ-VAE-2 has a top-level rate of $f = 32$ but requires three discrete latent codes to achieve this [41]. By introducing perceptual and adversarial loss terms, VQ-GAN [18] is able to achieve a compression rate of $f = 32$ with only a single discrete latent representation whilst maintaining high quality reconstructions [18]. However, the greater weighting on perceptual and adversarial loss does mean that VQ-GAN sometimes edits the reconstructions, rather than faithfully reconstruct the input. Later, improvements including differential data augmentation [3], codebook improvements, and a transformer-based architecture [60] improved reconstruction quality further, but still rely on adversarial components.

Designed for audio compression [61], residual VQ proposes the use of multiple codebooks to recursively quantize and refine the residual of the input. This produces multiple discrete representations, which can later be reconstructed by the decoder to recover the waveform. Individual codebooks can be dropped out, allowing for variable bit-rates [61]. Concurrently to our work, Lee et al. [32] used residual VQ to represent images with $f = 32$ and then trained a spatial transformer to autoregressively predict the stack of discrete tokens at a given spatial location, allowing for fast sampling even with multiple levels of discrete representations [32]. A summary of each VQ model and their latent and codebook sizes is shown in Table 1.

Model	Input Size	Latent Shape	Codebook Size	FID/val	FID/train
VQ-VAE	128×128	32×32	512	–	–
VQ-VAE-2	256×256	64×64 & 32×32	512	–	~ 10
	1024×1024	128×128 & 64×64 & 32×32	512	–	–
DALLE	256×256	32×32	8192	32.01	33.88
VQ-GAN	256×256	16×16	1024	7.94	10.54
	256×256	16×16	16384	4.98	7.41
	256×256	32×32	8192	1.49	3.24
	256×256	64×64 & 32×32	8192	1.45	2.78
RVQ-VAE	256×256	$8 \times 8 \times 2$	16384	–	10.77
	256×256	$8 \times 8 \times 4$	16384	–	3.20
	256×256	$8 \times 8 \times 8$	16384	–	2.69
	256×256	$8 \times 8 \times 16$	16384	–	1.83

Table 1: Summary of various vector-quantization (VQ) methods. The trend with VQ image models is increasing compression rates f and codebook sizes. However, to achieve these compression rates techniques such as perceptual and adversarial losses must be used.

A typical strategy for selecting which codebook vector e_i to map to a given embedding is to compute the Euclidean distance between the embedding and each codeword centroid, and then pick the $\arg\min$ [54], known as a k-means strategy. This can result in "codebook collapse", where certain codewords never get used, limiting the effective capacity of the model. An alternative is to use Gumbel-Softmax [25] to select codewords, which increases codebook utilisation but leads to worse reconstruction quality [3]. The issue of codebook collapse is significant and there have been a number of attempts to address it. [60] found that a lower codeword dimension and codeword normalization improved utilisation. [61] proposed setting a threshold for "stale" codes, and reinitialising them to a random vector from the current batch when they fall below this threshold. [32] proposed the sharing of a single codebook across many quantizers and stochastically sampling the codes as a function of their distance to each codeword centroid, rather than deterministically using the $\arg\min$.

All previously described approaches use VQ models to enhance existing AR models, primarily to improve sampling speeds by reducing the spatial dimension they operate over. Little work directly addresses the discrete prior model. Discrete diffusion models [1] are a NAR approach to generating discrete data, applied to VQ-GAN latents in Bond-Taylor et al. [3], resulting in fast sampling, flexible inpainting, and high fidelity outputs.

2.4 Step-unrolled Denoising Autoencoder

SUNDAE [44] is a NAR text generative model evaluated on three language modelling tasks: unconditional text-generation, inpainting of Python code, and machine translation – setting a new state-of-the-art among NAR models for the latter [44]. It is capable of fast sampling, producing high quality samples in as few as 10 steps.

It is trained using a denoising objective, akin to BERT's objective [57] but with multiple denoising steps. Given a uniform prior p_0 over some space $Z = \{1, \dots, v\}^N$ where N is the size of the space and v is the vocabulary size, consider the Markov process $\mathbf{z}_t \sim f_\theta(\cdot|\mathbf{z}_{t-1})$ where f_θ is a neural network parameterised by θ, then $\{\mathbf{z}_t\}_t$ forms a Markov chain. This gives a t-step transition function:

$$p_t(\mathbf{z}_t|\mathbf{z}_0) = \sum_{\mathbf{z}_1,\dots,\mathbf{z}_{t-1} \in Z} \prod_{s=1}^{t} f_\theta(\mathbf{z}_s|\mathbf{z}_{s-1}) \tag{2}$$

[44] and, given a constant number of steps T, our model distribution $p_T(\mathbf{z}_T|\mathbf{z}_0)p_0(\mathbf{z}_0)$ – which is clearly intractable.

Instead, SUNDAE uses an *unrolled denoising* training method that uses a far lower T than is used for sampling [44]. To compensate, they unroll the Markov chain to start from corrupted data produced by a *corruption distribution* $\mathbf{z}_0 \sim q(\cdot|\mathbf{z})$ rather than from the prior p_0 so the model during training sees inputs alike those seen during the full unroll at sample time [44]. Typically, $T = 2$ is used during training, as a single step would be similar to BERT's objective [13] which would not be performant as seen in earlier work using BERT as a random field language model [57].

The training objective of SUNDAE is the average of all cross-entropy losses on the chain after t steps, which is shown to form an upper bound on the actual negative log-likelihood [44]. Increasing T leads to a minor improvement in performance, but considerably slows down training [44] and increases memory usage.

One advantage of this approach is that sampling starts from random tokens, rather than a "masking" token [3, 1]. Unmasking approaches means that $T \leq N$ as at minimum, one token is unmasked per step. Additionally, it allows the model to "change its mind" about previously predicted elements during sampling, permitting fine-grained adjustments and correction of errors.

2.5 Hourglass Transformers

Vanilla transformers incur a memory complexity of $\mathcal{O}(L^2)$ for each block [56], dominated by costly multi-head self-attention mechanisms. Most research into efficient transformers focuses on improving the efficiency of the attention mechanisms using sparse attention patterns [8] or through linear complexity approximations [59].

Recent work has focused on making the architecture itself more efficient. Funnel transformers [11] progressively downsamples the input sequence and hence reduces the computational cost of the model. The saved floating point operations (FLOPs) can then be reassigned to create deeper or wider models and thus outperform vanilla transformers given the same computational budget [11]. However, the final layer does not operate at the same granularity as the input, making it unusable for tasks such as per-token classification or generative modelling. Hourglass transformers [36] include both up- and down-sampling mechanisms, resulting in a computational saving whilst being general-purpose models.

2.6 Summary of Trends in Deep Generative Modelling

Deep generative modelling research is a fast moving, complex and turbulent field to follow. Nonetheless, it is worthwhile to distil advancements into a selection of high level trends.

Improving quality and efficiency in non-adversarial generative models – GANs have long dominated as the pinnacle of sample quality and efficiency. Despite this, they are plagued by previously discussed issues, motivating research into non-adversarial approaches of equal quality to GANs. Certain non-adversarial solutions do beat GANs in quality, but GANs still dominate in terms of sample speed, making them the standard in real-world generative modelling applications – bar cutting edge applications [40, 19]. Hence, the trend is the simultaneous improvement in efficiency and quality, as it is clear that without both, adoption in practise will not occur. Satisfying these speed and quality requirements with a non-adversarial solution would in turn satisfy the aforementioned generative modelling trilemma [58].

Autoregressive to non-autoregressive models – NAR models offer a number of advantages over AR models as discussed in earlier sections. It is clear that NAR solutions will soon be a default over AR methods by observing that initial proposed methods and subsequent improvements often replace AR components with NAR components. For example: sampling VQ-GAN latents with AR transformers [18] to using discrete diffusion models [3]; DALL·E using AR sampling [40] to DALL·E 2 using diffusion models [19].

Class conditional to zero-shot conditional generative models – One especially popular trend is the shift from specifying a set of predefined classes when conditioning a model, to full zero-shot generation. This is usually realised by jointly learning text and image embeddings, then encoding a text prompt at sample time to condition the model [40, 19, 42, 32]. This allows for a much higher degree of creative control – an all too often overlooked property – and can be easily integrated with existing architectures. However, they require large amounts of labelled images and associated text prompts, usually scraped from the internet [42, 40, 19]. This makes bias and dangerous content introduced by the training data much harder to control and filter, influencing the resulting samples [34]. Nonetheless, it is clear that the natural language conditioning of generative models will persist.

Use of a vector-quantized discrete prior – Though VQ models have helped produce excellent results both within generative modelling [41, 18, 3, 42, 40, 60, 32] and elsewhere [61], excellent results can also be obtained without the use of them [7, 50, 21], especially with diffusion models [46, 47, 14, 48, 58, 51, 26, 17]. The advantage of using a VQ-based approach is the reduction of the spatial resolution that the generator model must operate over, aiding in scaling to higher resolutions and improving sampling speeds. However, the two-stage training approach can be unwieldy without pretrained VQ models and makes inpainting more involved. Additionally, they are plagued with issues such as codebook collapse [18, 3, 60], limiting the potential capacity of the model. It remains to be seen whether VQ models will continue being a popular component in generative modelling pipelines, or be rendered obsolete.

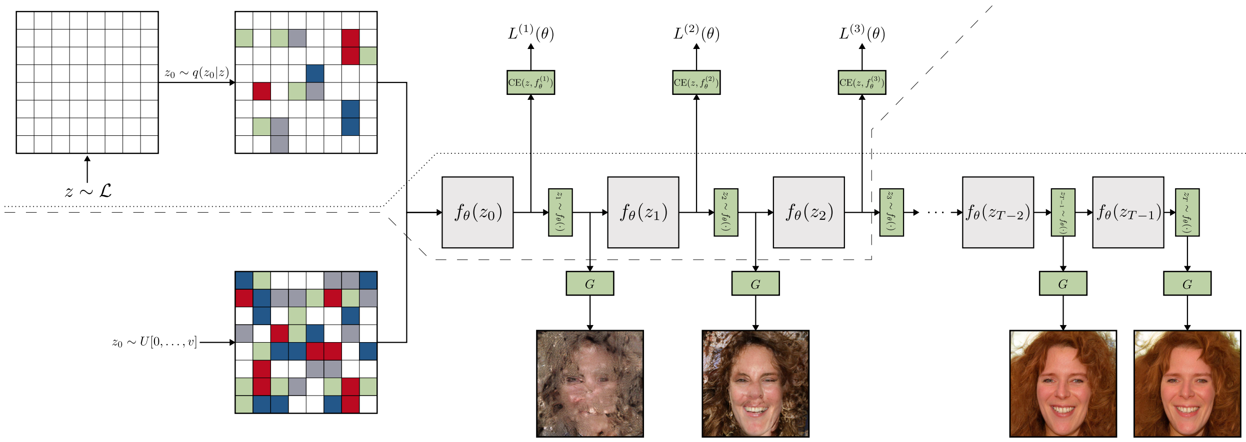

Figure 4: An overview of the SUNDAE training and sampling of discrete latent representations. Above the dashed line shows the training process, whereas below the dotted line shows the sampling process. The training process begins by sampling $\mathbf{z} \sim \mathcal{L}$ and then sampling from the corruption distribution $\mathbf{z}_0 \sim q(\mathbf{z}_0|\mathbf{z})$. SUNDAE then denoises for 2 to 3 steps, computing the cross-entropy loss at each step in the chain which is subsequently averaged to produce a final loss. Sampling begins by obtaining $\mathbf{z}_0$ from a uniform prior and iteratively denoising for T steps. At each step in the chain, the sample $\mathbf{z}_t$ can be decoded by the VQ-GAN decoder G to obtain $\mathbf{y}_t$.

3 Methodology

Our proposed method aims to push the efficiency of generative models to the limit via a combination of current techniques. To do so, we first use pretrained VQ-GANs from [18] to generate a dataset of discrete latent representations, described in §3.1. By operating at a latent level, we reduce the spatial resolution for our second stage generator. We implement our generator as a modified hourglass transformer, described in §3.2 and trained using a NAR method described in §3.4. This permits extremely fast sampling described in §3.5. To thoroughly test the efficiency and scalability of our approach, we train a megapixel VQ-GAN (described in §3.3) and repeat SUNDAE training and sampling on the resulting discrete latent representations. In §3.6, we explore flexible inpainting using our framework. An overview of training and sampling is shown in Figure 4, and of the latent dataset generation in Figure 3.

Each component represents the pinnacle of performance in their respective area: compression ratio in VQ image models with VQ-GAN, fast non-autoregressive sampling of discrete data with SUNDAE, and transformer scalability with our modified hourglass transformer. Together, we obtain an extremely efficient generative model that permits sampling at 1024×1024 resolution in seconds.

3.1 Latent Dataset Generation

We use the standard two-stage scheme for VQ image modelling [55, 41, 18, 3] using VQ-GAN [18] as a compression model. Where checkpoints are available, we use pretrained VQ-GANs for our experiments. For higher resolution experiments (FFHQ1024 [28]), pretrained models are not available and so the training our own VQ-GAN was necessary (see §3.3).

The second stage is to train a discrete prior model over the extracted latent representations. To enable this, we generated a latent dataset using a trained VQ-GAN. This allows for faster training of our discrete prior as the latent representations have been precomputed. A downside of this approach is that it limits the amount of data augmentation that can be applied to the dataset. We apply a simple horizontal flip to all images, effectively doubling the dataset size, with no other augmentation. Formally, given a dataset of images $\mathcal{X}$, a VQ-GAN encoder E with downsample factor f, and VQ codebook $\mathcal{C}$ with number of codewords v, trained on $\mathcal{X}$, we define our latent dataset $\mathcal{L}$ as:

$$\mathcal{L} = \{\mathcal{C}(E(\mathbf{x})) \mid \mathbf{x} \in \mathcal{X}\} \tag{3}$$

where $\mathbf{x} \in \mathbb{R}^{3\times H\times W}$ is a single element of the augmented image dataset $\mathcal{X}$ and $\mathbf{z} = \mathcal{C}(E(\mathbf{x})) \in \{1, \ldots, v\}^{h\times w}$ is the corresponding discrete latent representation. In other words, each $f \times f$ patch in $\mathbf{x}$ is mapped to a single discrete value from 1 to v (corresponding to a codeword $\mathbf{e} \in \mathcal{C}$), resulting in a latent representation of shape $\frac{H}{f} \times \frac{W}{f} = h \times w$.

We then use $\mathcal{L}$ to train a discrete prior over the latents. Coupled with the VQ-GAN decoder G, we obtain a powerful generative model by first sampling $\mathbf{z}_0$ from a uniform prior distribution, iteratively denoising using SUNDAE, and then decoding $\mathbf{z}_T$ using the VQ-GAN decoder G to obtain the final sample $\mathbf{y}$. The training of this discrete prior model forms the bulk of our work in this paper.

3.2 2D-Aware Hourglass Transformer

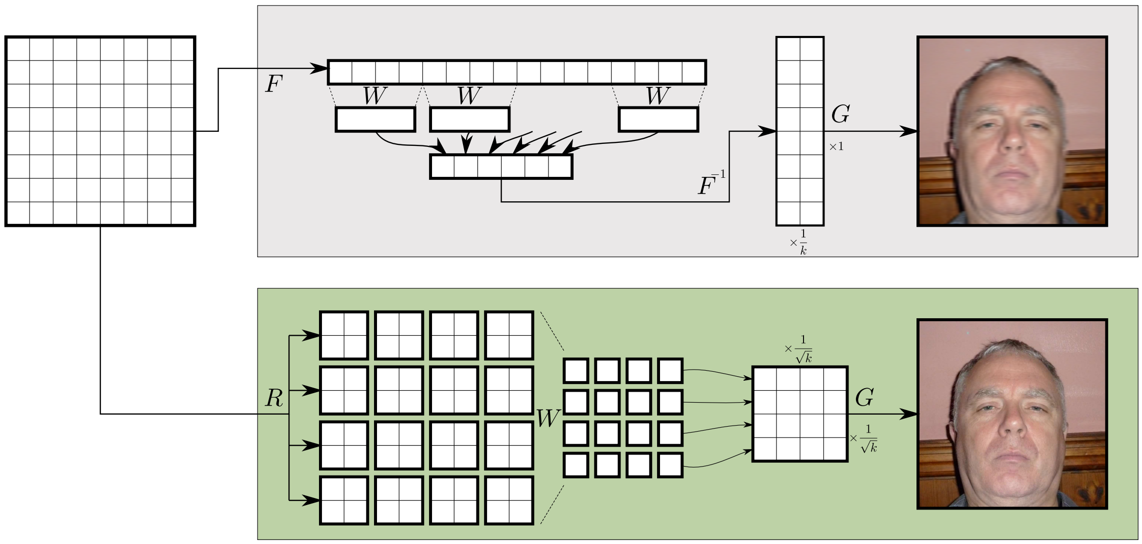

Figure 5: **Top:** Showing the effect of resampling sequence embeddings using original formulation. Resampling will be applied to only one axis, resulting in resampling in only one axis of the decoded image. **Bottom:** Our method of resampling, extracting two-dimensional patches of size $\sqrt{k}$, then resampling. The sequence is then flattened and passed to subsequent transformer layers.

Inspired by successes in hierarchical transformers for language modelling [36], we modify their architecture for use with discrete latent representations. We will later use this architecture to implement a discrete prior over the VQ-GAN latents. Hourglass transformers have been shown to efficiently handle long sequences, outperform existing models using the same computational budget, and meet the same performance as existing models more efficiently by using an explicit hierarchical structure [36]. The same benefits should also apply to VQ image modelling.

However, the design and parameters chosen by the original authors are tailored for language modelling [36] with limited experiments on image generation. We believe that we can improve upon their architectural choices for the task of discrete latent modelling. Some changes may also be applicable to pixel-level generation. In this subsection, modifications to the architecture are outlined.

2D-Aware Downsampling – The original formulation of hourglass transformers [36] introduced up- and down-sampling layers, allowing the use of hierarchical transformers in tasks that have equal input and output sequence lengths. However, we found certain flaws in their original formulation that hinders performance on multi-dimensional inputs.

In their work, resampling is applied to the flattened embedding sequences, meaning that a corresponding two-dimensional vector-quantized image is resampled more in one axis compared to the other. In their work they did not address this, except for experiments on ImageNet [43] (downsampled to 32×32) where they resampled with a rate of $k = 3$, corresponding to three colour channels. However, if they were to resample again by nesting the hourglass transformers, the issue of one spatial dimension being downsampled more than others would arise.

In our formulation, we reshape the flattened sequence into a two-dimensional form and apply resampling equally in the last two axes. With a resampling rate of k we apply $\sqrt{k}$ in each spatial axis – evenly distributing the resampling among the axes. In our preliminary experiments, this significantly improved the performance of the discrete prior model, and suspect the same approach could improve performance on any multi-dimensional data, which we leave for future work to confirm. A comparison between the previous approach and our amended solution is shown in Figure 5.

For our resampling operations, we use linear resampling (following recommendation by Nawrot et al. [36] to use linear resampling for image tasks) and a post-resampling attention layer, providing global context and aggregation of information to the resampling operations [36]. Our adjusted resampling method is as follows:

$$h' = A(\boldsymbol{W}^{(\intercal)} \cdot R(\boldsymbol{h}) + \boldsymbol{r}), \quad \boldsymbol{W} \in \mathbb{R}^{\frac{(d \cdot h \cdot w)}{k} \times (d \cdot h \cdot w)} \tag{4}$$

where A is the post-resampling attention layer, $\boldsymbol{h}$ is the current hidden state, $\boldsymbol{r}$ is the residual (with $\boldsymbol{r} = \boldsymbol{0}$ when downsampling), R is the modified reshape operation, d is the hidden layer dimension, and $\mathbf{W}$ is a learned projection matrix. The reshape operation R was implemented as a space-to-depth operation followed by combining the feature and depth dimensions.

Rotary Positional Embeddings – Transformers have no inductive biases that allow it inherently know the position of an element in the sequence. Embeddings that represent positions must be injected into the model in addition to the input itself. In our work, we choose to use rotary positional embeddings [49] as they require no additional parameters, incur only a small runtime cost, and can be easily extended to the multi-dimensional case [2], which we exploit here. Though transformers are clearly capable of learning that elements far apart in a flattened sequence may be semantically close, we found that explicitly extending positional embeddings to the multi-dimensional case to provide a modest boost in performance and improve the rate of training convergence. The original hourglass transformer on pixel-wise generation also opted to use rotary embeddings [36] but in the single dimensional case. They note also that rotary embeddings have the advantage of being compatible with any self-attention mechanism.

Removal of Causal Constraints – In the original AR formulation of hourglass transformers they noted that naively resampling could cause information leakage into future sequence elements – therefore violating the autoregressive property [36]. As our approach is NAR we do not make any special considerations to avoid information leaking into the future. This simplifies the model by avoiding shifting and causal masking operations required in the original work.

3.3 Training a megapixel VQ-GAN

Training at higher resolutions means greater computational requirements and slower sampling speeds. With an AR model, the sampling time can be immense as it scales linearly with data dimensionality, even with an auxiliary VQ image model [18]. With a NAR model however, the sampling speed is explicitly controlled and does not directly grow as a function of input size – excluding the increase in time for one network pass from using a larger model on a larger input.

We trained a larger variant of VQ-GAN with $v = 8192$ operating on 1024×1024 from FFHQ1024. To our knowledge, this is the highest resolution dataset VQ-GAN has been applied to [18]. Once trained, we generate the latent dataset as before, the only difference being an increased sequence length – greater than SUNDAE was ever tested on in the original work [44]. Specifically, we obtain a downsampling rate of $f = 32$, resulting in discrete latents of size $32 \times 32 = 1024$.

The resulting reconstructions are overall of good quality given the large compression ratio in use. However, the reconstructions are not without artifacts. Figure 6 shows examples of particularly prevalent artifacts including occasional unrealistic textures in hair (middle reconstruction) and corruption of text (right reconstruction). The corruption of text is a common issue in VQ image models [40], and the unrealistic textures are a result of the extreme compression rate or a lack of model capacity.

VQ-GAN is trained to minimise the mean absolute error, perceptual loss, and adversarial loss [18] in addition to a k-means VQ loss. Specifically, VQ-GAN is trained to minimise the following loss:

$$\begin{aligned}
L_{\text{PIX}} &= \alpha_{\text{PIX}} \cdot |\mathbf{x} - \hat{\mathbf{x}}| \cdot \\
L_{\text{VQ}} &= \alpha_{\text{VQ}} \cdot \left(||\hat{\mathbf{z}} - \mathbf{z}||^2 + ||sg[E(x)] - \mathbf{z}||_2^2 + ||E(x) - sg[\mathbf{z}]||_2^2\right) \\
L_{\text{GAN}} &= \alpha_{\text{GAN}} \cdot (\log D(x) + \log(1 - D(\hat{x}))) \\
\lambda &= \frac{\nabla_{G_{-1}}[L_{\text{PIX}} + L_{\text{PER}}]}{\nabla_{G_{-1}}[L_{\text{GAN}}] + \epsilon} \\
L &= L_{\text{VQ}} + \lambda \cdot L_{\text{GAN}} \\
\alpha_{\text{PIX}} &= 1.0,\ \alpha_{\text{VQ}} = 1.0,\ \alpha_{\text{GAN}} = 0.5,\ \alpha_{\text{PER}} = 1.0
\end{aligned} \tag{5}$$

[18] where our discriminator is implemented using three layers, perceptual loss L_{PER} implemented using a pretrained VGG16 model [45], $\nabla_{G_{-1}}[\cdot]$ is the gradient with respect to the last layer of the VQ-GAN decoder G, and $sg[.]$ is the stop-gradient operator [54]. The generator and discriminator model parameters are updated separately, as is standard procedure in GAN-based literature [18].

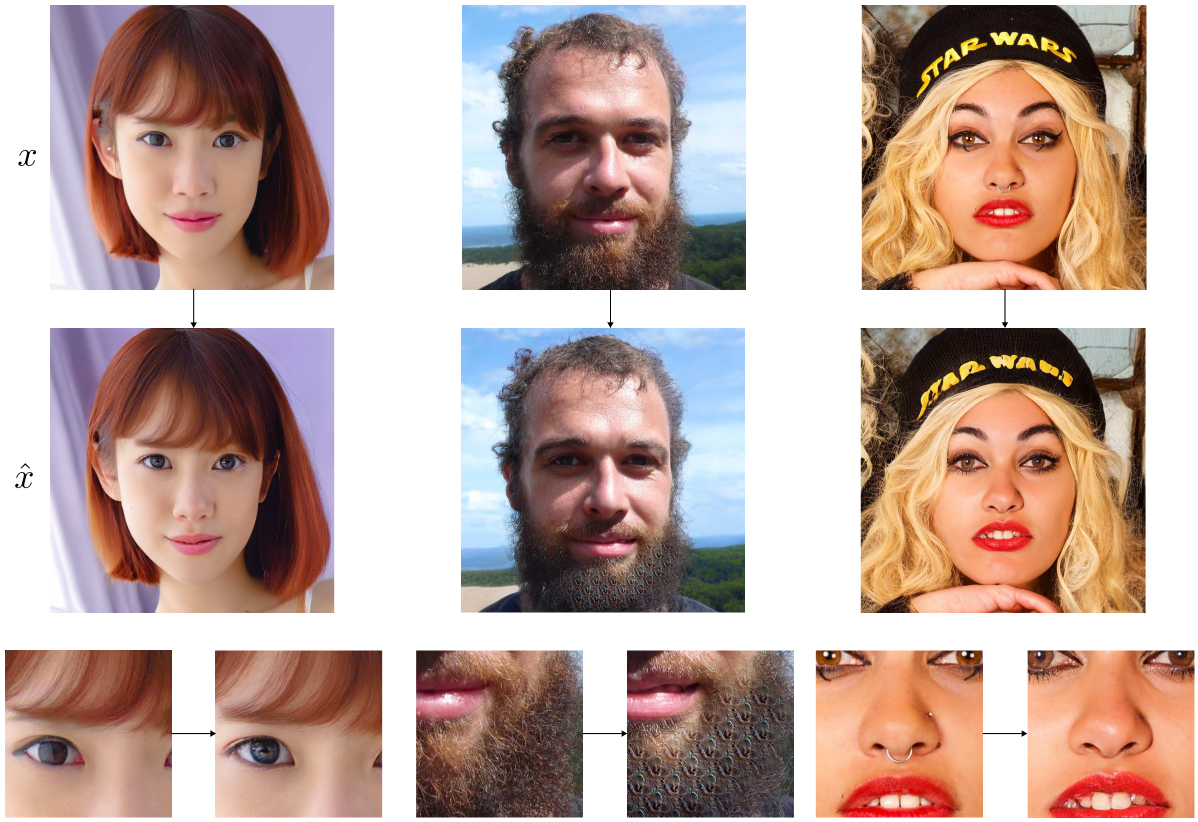

Figure 6: VQ-GAN does not always produce faithful reconstructions due to being optimised for perceptual quality rather than a direct error between the reconstructions and inputs. The top row contains example inputs, middle row contains resulting reconstructions, and the final row highlights points of interest that have been edited – some perceptually valid and others artifacts. **Left**: The eye colour has been brightened, and hair shifted to conceal an ear piercing, rather than reconstruct it. **Middle**: The most common reconstruction artifact occurs with certain types of hair, where a repeating and unrealistic texture appears. The pose of the lip is also altered. **Right**: Another common artifact where text in images is corrupted. This is common in VQ models. Additionally, the model removes nose and lip piercings, in addition to altering eye makeup. This is again a valid image, but is not a faithful reconstruction.

This means there is less of a weight on directly minimising the pixel-wise error between the input and reconstruction. This gives rise to an interesting property of VQ-GAN where the reconstructions may be perceptually valid but distinct from the input. The left reconstruction in Figure 6 demonstrates this with a change in eye colour and a shift in hair position – concealing an ear-piercing. This even more apparent in the right reconstruction where all piercings are flawlessly removed – along with adjustments to eye makeup.

Using VQ image models to compress images further whilst retaining high quality and faithful reconstructions remains an open and challenging area of research – particularly true at high resolutions. In our preliminary experiments, we found a higher f led to the majority of reconstructions being of an untenable quality. Conversely, decreasing f led to latent representations of sizes that resulted in large memory requirements in the downstream SUNDAE prior, making inference on consumer-grade GPUs impractical.

Training VQ-GAN at this resolution and at our chosen downsampling rate is extremely computationally expensive. In our configuration we were limited to a global batch size of 4 across four 32 GiB Tesla V100 GPUs. This made a full hyperparameter sweep of VQ-GAN's parameters not possible. Therefore, we accepted good reconstructions on average with occasional artifacts that could potentially manifest in the final samples. Improving the effectiveness of VQ image models is not the focus of this research project. We found these artifacts to only appear rarely in the final samples, shown in §4.1.

3.4 Non-Autoregressive Generator Training

We train a SUNDAE model on the flattened (in a raster-scan format) VQ latents $\mathbf{z} = \{\mathbf{z}^{(0)}, \ldots, \mathbf{z}^{(N)}\}$ where $N = h \cdot w$. The function $f_\theta(\cdot)$ is implemented using our proposed 2D-aware hourglass transformer.

Given a latent $\mathbf{z} \sim \mathcal{L}$, we apply our corruption distribution. This is done by first sampling a corruption threshold vector t with $t_i \sim U[0, 1]$ and a random matrix $\mathbf{R}$ of the same shape as $\mathbf{z}$ where $R_{i,j} \sim U[0, 1]$. Using this, we construct a mask matrix $\mathbf{M}$ with $M_{i,j} = 1$ when $R_{i,j} < t_i$ and $M_{i,j} = 0$ otherwise. This results in $\mathbf{M}_i$ having approximately t_i of its entries be 1.

Then, given $\mathbf{z}_0 \sim p_0$, we update the $\mathbf{z}_0$ to start unrolled denoising from:

$$\mathbf{z}_0 \leftarrow \mathbf{M} \cdot \mathbf{z}_0 + (\mathbf{1} - \mathbf{M}) \cdot \mathbf{z}. \tag{6}$$

We then iteratively unroll the current sample $\mathbf{z}_{t-1}$ to obtain $\mathbf{z}_t$ for steps $t \in \{1, \ldots, T\}$. To perform one unroll step, simply compute logits $f_\theta(\mathbf{z}_t|\mathbf{z}_{t-1})$ and then sample from the resulting distribution to obtain $\mathbf{z}_t$, storing the logits at each step t. Then, compute the cross entropy loss between all logits at each t and the target $\mathbf{z}$. This differs from some NAR solutions which predict the corruption noise ϵ [22] rather than the target. The mean of the cross entropy losses is then computed to produce the final loss:

$$L^{(1:T)}(\theta) = \frac{1}{T}\left(L^{(1)}(\theta) + \cdots + L^{(T)}(\theta)\right) \tag{7}$$

as in §2.4, which allows for the backpropagation of gradients and consequently the updating of parameters θ. Though the default $T = 2$ is sufficient, we found $T = 3$ to result in more diverse samples and so used it in all latent sampling experiments.

An alternative corruption distribution would be to instead use a deterministic method $\mathbf{z}_0^{(i)} = \texttt{[MASK]} = v + 1$, essentially replacing all tokens with $M_{i,j} = 1$ with a special masking token. This is similar to "progressive unmasking" of latents used in prior work [3, 1]. This strategy was not considered as the use of a masking token places an upper bound on T during sampling (updating at most one token per step) as well as not allowing for self-correction, as once a token is unmasked it becomes fixed [3, 1].

3.5 Generating High-Resolution Images

During sampling, we sample $\mathbf{z}_t \sim f_\theta(\mathbf{z}_t|\mathbf{z}_{t-1})$ for a constant number of steps T, beginning randomly from $\mathbf{z}_0$ sampled from a uniform distribution [44]. The original work proposed a number of improved strategies for sampling in a smaller number of steps, including low-temperature sampling and updating a random subset of tokens [44] rather than all simultaneously.

Sampling with a lower temperature, however, reduces the diversity of the outputs. To alleviate this, we anneal the temperature down from a high value (≈ 1.0) down to a low value during the sampling process. We found this retained the fast sampling speed whilst improving diversity.

In certain latent sampling configurations, updating only a random subset of tokens also helps improve diversity. Savinov et al. [44] used this strategy when performing low-temperature sampling. However, we found that for low-step sampling ($T < 20$) that all tokens must be able to be updated in order to produce meaningful samples before the maximum number of steps is reached. Hence in these cases, we do not follow their proposal and instead use a high sample proportion (0.7-1.0). In scenarios where we are permitted a time-budget allowing for many sampling steps, the sample proportion can be freely reduced for an increase in sample diversity.

Additionally, if an individual sample does not change between step $t - 1$ and t, it is prevented from being changed further. If all samples are frozen, sampling terminates early, provided a minimum number of steps have been completed. This improves the sampling speed with little cost to the sample quality. This is significant when performing large-batch sampling or when the maximum number of steps is large.

Once sampling has terminated, the sampled latent code $\mathbf{z}_T$ is decoded by G to produce a final sample $\mathbf{y}$. In fact, any $\mathbf{z}_i$ in the Markov chain is a valid input to G. Decoding during sampling and visualising $\mathbf{y}_t$ each step t shows the model gradually denoising the latent and correcting errors accumulated during the sampling.

3.6 Arbitrary Pattern Inpainting

As noted in the original work [44] and other NAR solutions [3], one advantage of NAR models is that they are not limited to causal inpainting. They support arbitrary inpainting masks and draw upon context from $\mathbf{z}_{t-1}$, rather than

$\mathbf{z}_{t-1}^{<i}$, enabling them to easily perform inpainting tasks that are complex to implement with AR models. This property also results in higher quality and more diverse samples [3].

The inpainting procedure takes an image $\mathbf{y} \in \mathbb{R}^{H \times W \times 3}$ and a pixel-level binary mask $m_p \in \{0,1\}^{H \times W}$ as input. By taking $f \times f$ regions of m_p and applying a logical `AND` in them, we obtain a latent level mask $m_{\text{vq}} \in \{0,1\}^{h \times w}$. We encode $\mathbf{x}$ using E to obtain $\mathbf{z}$, and then initialise our starting latent $\mathbf{z}_0$ by randomly setting points in $\mathbf{z}$ where $m_{\text{vq}} = 1$, and keeping $\mathbf{z}$ the same when $m_{\text{vq}} = 0$. We then sample starting from $\mathbf{z}_0$, allowing the model full context, but only update regions that were masked according to m_{vq}. We use a lower temperature for inpainting ($0.3 \leq \tau \leq 0.5$). Decoding $\mathbf{z}_T$ with G produces the final result $\mathbf{y}$, identical to the end of the sampling process.

Sampling at a latent level means the model is unable to do fine-grained inpainting at a pixel level. The definition of the VQ mask m_{vq} means that some pixels outside the mask may be altered if the pixel mask is not perfectly aligned with the VQ mask (when `AND` does not always receive all 0s or all 1s). We found in practise this had little effect on the perceptual quality of the outputs.

Implementation Details

Dataset	**FFHQ256**	**FFHQ1024**	**CelebA**	**MNIST**	**FashionMNIST**	**ImageNet**
Dataset Size	$60,000$	$60,000$	$190,000$	$60,000$	$60,000$	1.28M
Codebook Size	1024	8192	1024	256	256	1024
Latent Shape	16×16	32×32	16×16	28×28	28×28	16×16
Unroll Steps	3	3	3	2	2	3
Depth	$3-10-3$	$2-12-2$	$2-12-2$	$2-8-2$	$2-8-2$	$3-14-3$
Dimension	1024	1024	1024	1024	1024	1024
Shorten Factor	4	4	4	4	4	4
Attention Heads	8	8	8	8	8	12
Resample Type	Linear	Linear	Linear	Linear	Linear	Linear
Classes	–	–	–	10	10	1000
Class Dimension	–	–	–	1024	1024	1024

Table 2: Table of parameters for all training experiments. Depth is represented as three numbers corresponding to number of layers before downsampling, number of downsampled layers, and number of layers after upsampling. The dataset size is the size of the training split of the dataset. The latent shape of MNIST experiments is exactly equal to the shape of $\mathbf{x}$, as for these experiments we operate directly on a (discrete) pixels.

All SUNDAE models are trained using the Adam optimizer [29] as realised in its AdamW implementation in PyTorch [39]. Similarly, all models and training scripts are implemented in PyTorch. For unconditional generation on 256×256 images, training was done on a single 24 GiB Nvidia RTX TITAN. For unconditional generation on 1024×1024 images, training was done on a single 32 GiB Nvidia V100. Finally, for conditional generation on ImageNet, training was done on a single 80 GiB Nvidia A100. All parameters used for training the SUNDAE models are shown in Table 2.

4 Evaluation

4.1 Unconditional Image Generation

We evaluate our method on the task of unconditional image generation on datasets FFHQ256, FFHQ1024, and CelebA. We use pretrained VQ-GAN checkpoints provided by the original VQ-GAN authors [18] for 256×256 experiments. We evaluate our models using FID Infinity [10], coverage, and density [35], plotting how these metrics change as number of sampling steps T (Figure 7), sampling temperature τ (Figure 8), and sample proportion (Figure 9) are varied. Additionally, we show representative unconditional samples in Figures 1 & 10 and dataset nearest neighbours in Figure 11 to demonstrate sample diversity and quality.

Figure 7 demonstrates a surprising property of our model: additional steps during the sampling process do not improve sample quality further. It is important to note that this only holds if the other parameters remain fixed. Therefore, the results do not suggest that additional sampling steps are detrimental to performance, as a low number of steps will clearly result in poor quality results. Rather, it indicates that merely adding more sampling steps is not sufficient in our framework, and other parameters must also be adjusted to reflect changes in T.

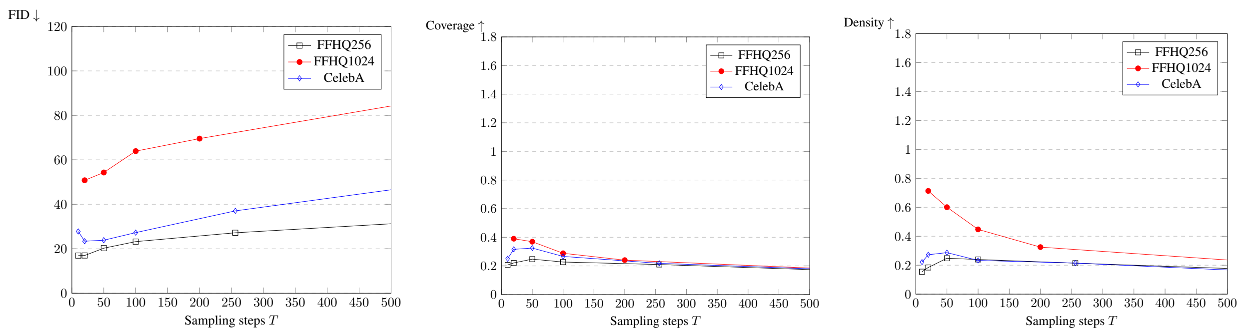

(a) Steps vs. FID. (b) Steps vs. Coverage. (c) Steps vs. Density.

Figure 7: Plots showing sample quality in terms of different metrics as number of sampling steps T increases. Counter-intuitively, the sample quality decreases with number of sampling steps, seen on all metrics and datasets.

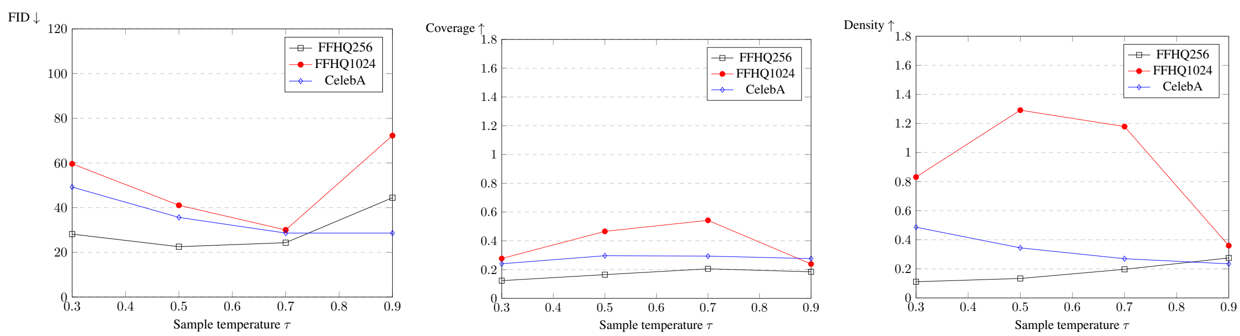

(a) Temperature τ vs. FID. (b) Temperature τ vs. Coverage. (c) Temperature τ vs. Density.

Figure 8: Plots showing sample quality in terms of different metrics as sample temperature τ is changed. Given the other parameters, a good choice of τ falls in the range $0.5 - 0.7$. However, this range may differ depending on the values of other parameters.

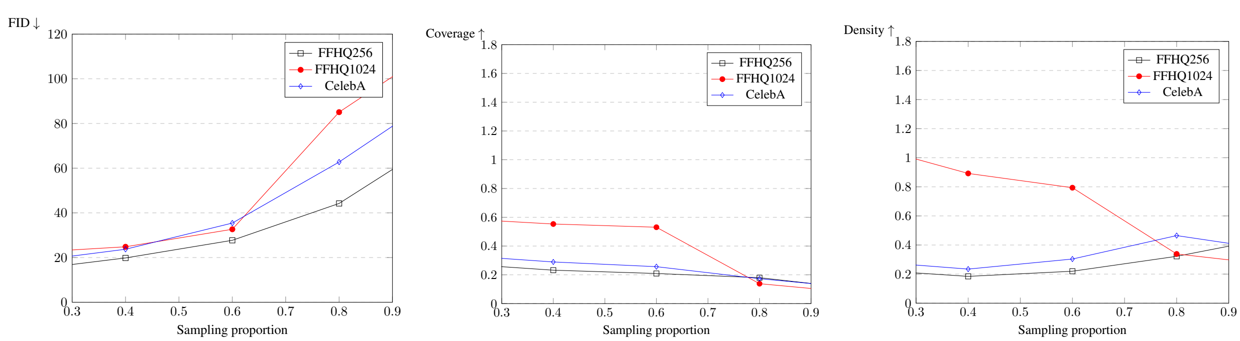

(a) Sample proportion vs. FID. (b) Sample proportion vs. Coverage. (c) Sample proportion vs. Density.

Figure 9: Plots showing sample quality in terms of different metrics as sample proportion is changed. Lower values seem to perform better given the other parameters, but again the optimal range may differ if other parameters are adjusted.

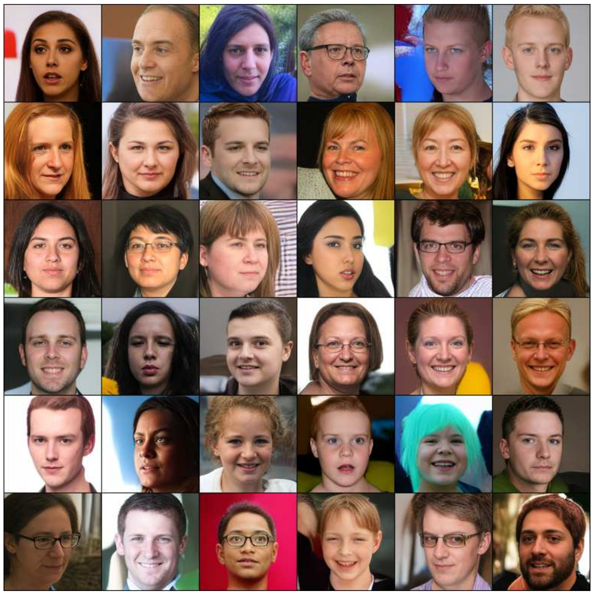

(a) Non-cherry picked batch of samples from the model trained on FFHQ256.

(b) Non-cherry picked batch of samples from the model trained on CelebA.

Figure 10: Unconditional generation on 256×256 face datasets.

Figure 11: FFHQ256 samples and their nearest neighbours in the dataset, based on LPIPS perceptual loss. Left-most column is a sample from our trained model, followed then by nearest neighbours, increasing in distance from left-to-right.

Figure 8 shows that picking a temperature in the range of 0.5 to 0.7 leads to the best sample quality across a large set of samples, at the cost of reduced diversity. Our model is capable of sampling with a higher temperature but is becomes more likely to generate corrupted examples as τ increases. Figure 9 confirms the result in Savinov et al. [44] that sampling with a lower proportion leads to higher sample diversity. However, in low-step scenarios, low proportions cannot be used effectively as the majority of elements in $\mathbf{z}_T$ will not have had enough opportunities to update, resulting in low quality outputs.

The samples shown in Figures 1 & 10 demonstrate that our model is capable of generating high quality and diverse samples. Our aim was to push the efficiency of generative models to their limit, however we were still surprised at precisely how fast the model could sample – particularly on megapixel scale experiments. The samples in Figure 1 were created in two seconds on a GTX 1080Ti. This can be further improved with more powerful accelerators, further optimisation, and model compilation. This kind of speed is unparalleled; significantly faster than prior non-adversarial solutions at this resolution. Additionally, our success here demonstrate the scalability of SUNDAE to sequence lengths of $N = 1024$, significantly larger than the maximum length tested in the original work ($N = 128$).

4.2 Conditional Image Generation

(a) 256×256 successful samples from the class "Valley".

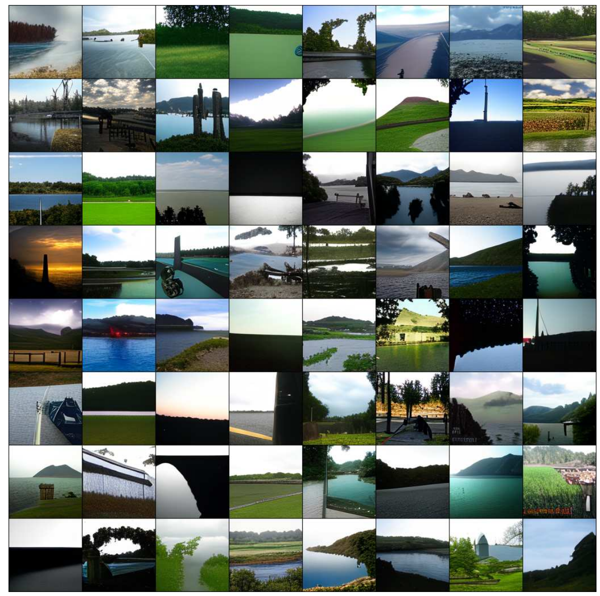

(b) 256×256 successful samples from the class "Lakeside".

(c) 256×256 failed samples from the class "King Penguin".

(d) 256×256 failed samples from the class "Giant Panda".

Figure 12: Examples of class-conditioned generation on ImageNet256 using $T = 50$ sampling steps. Top row contains examples of successful samples whereas bottom row contains failed samples. The contents of the failed samples resemble the target class, but are of low quality.

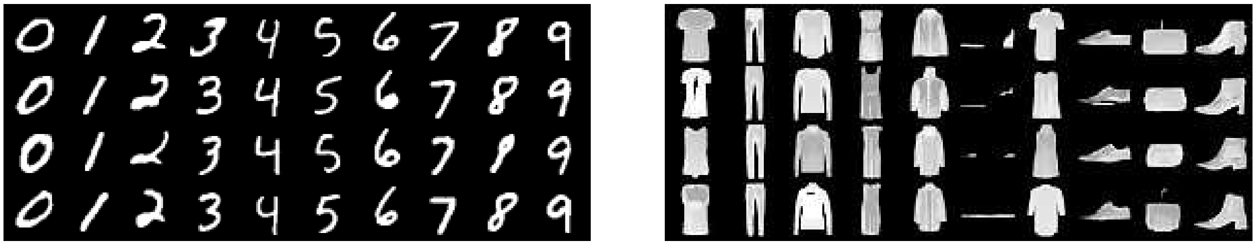

(a) Conditional, pixel-wise generation on MNIST.

(b) Conditional, pixel-wise generation on Fashion-MNIST.

Figure 13: Testing conditional generation using MNIST-style datasets. Coherent samples demonstrate that the proposed conditioning method does inject class information.

Another critical component of an ideal generative model is the ability to control its generation. We explore class-conditioned image generation of ImageNet at 256×256 resolution, using the pretrained ImageNet256 VQ-GAN checkpoints provided in the original work [18].

There are many valid ways of injecting a conditioning signal into generative models, for example passing one-hot or embedding class vectors. We use a simple solution proposed in [37]: adding a learned class embedding to every input embedding. To test whether their proposed method can also be applied to SUNDAE, we conducted an experiment on discrete MNIST-style datasets. We treat each of the possible 8-bit greyscale colour values as a codebook index, resulting in $v = 256$ – generating pixels directly rather than image patches. Results of these experiments are shown in Figure 13 and demonstrate that SUNDAE can incorporate conditional information using this simple approach.

Despite this, our model fails to produce reasonable samples for all classes in ImageNet. On classes containing large scenes such as landscapes, the samples are convincing and diverse. However, for classes requiring fine-grained detail, the outputs merely resemble the target class. Results of conditional generation with four representative classes are shown in Figure 12. Due to this, we chose not to compute perceptual metrics for conditional experiments as the sample quality was clearly insufficient via inspection alone. This could be a result of lack of model capacity, lack of training time, or the conditioning strategy tested on MNIST being insufficient for ImageNet. The training of a more effective conditional model is left for future work.

4.3 Arbitrary Image Inpainting

As outlined earlier, non-autoregressive generative models have a number of advantages on inpainting tasks, including supporting arbitrary masks and being able to use the full context available to them. We provide a number of examples of inpainting on FFHQ1024, showcasing different patterns and results given the same starting image and mask. As our method utilises a VQ image model, it is incapable of doing fine-grained inpainting at a pixel level. We found in practise this had little effect on the perceptual quality of the outputs, as shown in Figures 14a, 14b & 14c.

4.4 Limitations

As a result of our evaluation, some limitations of our approach arise. One weakness is that our VQ image model utilises adversarial components within it. This potentially means that each image patch (corresponding to each codebook entry) could suffer from mode collapse issues. However, our resulting samples are still diverse, suggesting that patch-wise mode collapse did not have a significant effect on the final samples.

We encountered great instability during training of the large VQ-GAN which led to many failed experiments. Additionally, the extreme compression ratio in the large VQ-GAN model occasionally resulted in unrealistic artifacts. Though most reconstructions are of good quality, the artifacts did rarely appear in the samples. Further research into high compression VQ models that do not use adversarial components remains an open and challenging area of research. When such a VQ model is designed, it can easily be substituted into our proposed framework.

Despite our model demonstrating extremely fast sampling it falls short of many recent methods in terms of perceptual quality metrics [3]. Though measures of perceptual quality such as FID are known to be flawed [10], other measures such as density and coverage also show inferior sample quality [35]. This is especially true on ImageNet where many classes merely resemble the target class – though this is likely due to lack of model capacity and training time. Despite this, the resulting samples on the FFHQ datasets are still very diverse and of excellent perceptual quality. Further work, particularly extensive parameter sweeps, is needed to improve quality in terms of these perceptual metrics.

(a) A large example of inpainting on a 1024×1024 image using our model.

(b) Multiple results of inpainting using the same block mask.

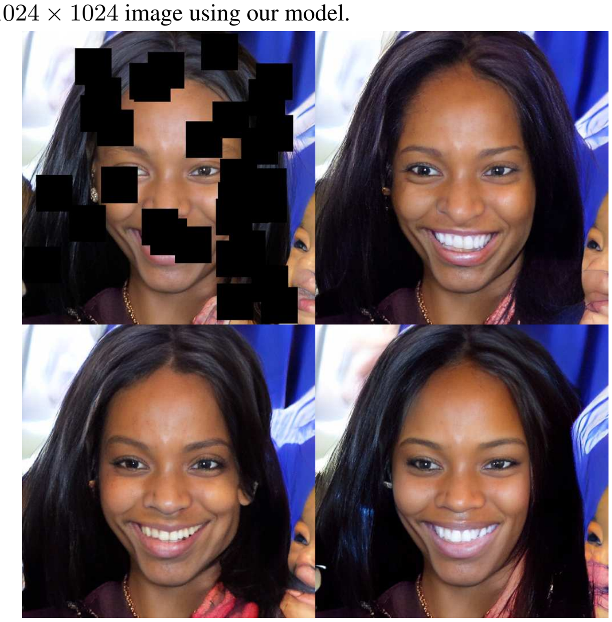

(c) Multiple results of inpainting on the same random mask.

Figure 14: Inpainting results on FFHQ1024. We compute multiple outputs per input image and mask to demonstrate diversity of outputs. Inpainting using a VQ image model that cannot be applied perfectly at a pixel-level. Nevertheless, the model still produces many convincing outputs at very high resolutions.

5 Conclusion

In this work we investigated pushing the efficiency of generative models via the combination of various techniques, following the trend in generative modelling research of simultaneously improving quality and speed of sampling using non-adversarial approaches. We found that the combination of these techniques formed a fast image generation framework. To our surprise, the proposed method was faster and more scaleable than expected, able to be applied with ease to megapixel images, and generate samples at such resolutions in seconds – considerably faster than existing non-adversarial methods. Additionally, we found that previously proposed hourglass transformers are not optimally defined on multi-dimensional inputs and subsequently proposed adjustments to them. We also demonstrated the scalability of SUNDAE by applying it to sequences of length 1024 – eight times longer than evaluated on in the original work. Our work demonstrates the superiority of the non-autoregressive paradigm, and joins a rapidly growing space of research into their use as a viable alternative to autoregressive frameworks. Additional research is needed into better VQ image models and into a stronger conditional generative model.

REFERENCES

[1] Jacob Austin, Daniel D. Johnson, Jonathan Ho, Daniel Tarlow, and Rianne van den Berg. Structured denoising diffusion models in discrete state-spaces, 2021. 4, 6, 7, 12

[2] Stella Biderman, Sid Black, Charles Foster, Leo Gao, Eric Hallahan, Horace He, Ben Wang, and Phil Wang. Rotary embeddings: A relative revolution. blog.eleuther.ai/, 2021. [Online; accessed]. 10

[3] Sam Bond-Taylor, Peter Hessey, Hiroshi Sasaki, Toby P. Breckon, and Chris G. Willcocks. Unleashing transformers: Parallel token prediction with discrete absorbing diffusion for fast high-resolution image generation from vector-quantized codes, 2021. 2, 5, 6, 7, 8, 12, 13, 17

[4] Sam Bond-Taylor, Adam Leach, Yang Long, and Chris G. Willcocks. Deep generative modelling: A comparative review of vaes, gans, normalizing flows, energy-based and autoregressive models. *IEEE Transactions on Pattern Analysis and Machine Intelligence*, pp. 1–1, 2021. ISSN 1939-3539. doi: 10.1109/tpami.2021.3116668. URL http://dx.doi.org/10.1109/TPAMI.2021.3116668. 3

[5] Andrew Brock, Jeff Donahue, and Karen Simonyan. Large scale gan training for high fidelity natural image synthesis, 2018. URL https://arxiv.org/abs/1809.11096. 4

[6] Xi Chen, Nikhil Mishra, Mostafa Rohaninejad, and Pieter Abbeel. Pixelsnail: An improved autoregressive generative model, 2017. 2, 4, 5

[7] Rewon Child. Very deep vaes generalize autoregressive models and can outperform them on images, 2020. URL https://arxiv.org/abs/2011.10650. 4, 7

[8] Rewon Child, Scott Gray, Alec Radford, and Ilya Sutskever. Generating long sequences with sparse transformers. *arXiv preprint arXiv:1904.10509*, 2019. 7

[9] Kyunghyun Cho, Bart van Merrienboer, Dzmitry Bahdanau, and Yoshua Bengio. On the properties of neural machine translation: Encoder-decoder approaches, 2014. 4

[10] Min Jin Chong and David Forsyth. Effectively unbiased fid and inception score and where to find them. In *Proceedings of the IEEE/CVF conference on computer vision and pattern recognition*, pp. 6070–6079, 2020. 13, 17

[11] Zihang Dai, Guokun Lai, Yiming Yang, and Quoc V. Le. Funnel-transformer: Filtering out sequential redundancy for efficient language processing, 2020. 7

[12] Cyprien de Masson d'Autume, Mihaela Rosca, Jack Rae, and Shakir Mohamed. Training language gans from scratch, 2019. URL https://arxiv.org/abs/1905.09922. 4

[13] Jacob Devlin, Ming-Wei Chang, Kenton Lee, and Kristina Toutanova. Bert: Pre-training of deep bidirectional transformers for language understanding, 2019. 5, 6

[14] Prafulla Dhariwal and Alex Nichol. Diffusion models beat gans on image synthesis, 2021. 2, 4, 7

[15] Laurent Dinh, David Krueger, and Yoshua Bengio. Nice: Non-linear independent components estimation. *arXiv preprint arXiv:1410.8516*, 2014. 4

[16] Laurent Dinh, Jascha Sohl-Dickstein, and Samy Bengio. Density estimation using real nvp. *arXiv preprint arXiv:1605.08803*, 2016. 4

[17] Tim Dockhorn, Arash Vahdat, and Karsten Kreis. Score-based generative modeling with critically-damped langevin diffusion, 2021. URL https://arxiv.org/abs/2112.07068. 4, 7

[18] Patrick Esser, Robin Rombach, and Björn Ommer. Taming transformers for high-resolution image synthesis, 2021. 2, 5, 7, 8, 10, 13, 17

[19] Aditya Ramesh et al. Hierarchical text-conditional image generation with clip latents, 2022. URL https://cdn.openai.com/papers/dall-e-2.pdf. 7

[20] Ian J. Goodfellow, Jean Pouget-Abadie, Mehdi Mirza, Bing Xu, David Warde-Farley, Sherjil Ozair, Aaron Courville, and Yoshua Bengio. Generative adversarial networks, 2014. 2, 4

[21] Louay Hazami, Rayhane Mama, and Ragavan Thurairatnam. Efficient-vdvae: Less is more. *arXiv preprint arXiv:2203.13751*, 2022. 7

[22] Jonathan Ho, Ajay Jain, and Pieter Abbeel. Denoising diffusion probabilistic models, 2020. 2, 4, 12

[23] Sepp Hochreiter and Jürgen Schmidhuber. Long short-term memory. *Neural Computation*, 9(8):1735–1780, 1997. 4

[24] Emiel Hoogeboom, Alexey A Gritsenko, Jasmijn Bastings, Ben Poole, Rianne van den Berg, and Tim Salimans. Autoregressive diffusion models. *arXiv preprint arXiv:2110.02037*, 2021. 4

[25] Eric Jang, Shixiang Gu, and Ben Poole. Categorical reparameterization with gumbel-softmax, 2016. 6

[26] Alexia Jolicoeur-Martineau, Ke Li, Rémi Piché-Taillefer, Tal Kachman, and Ioannis Mitliagkas. Gotta go fast when generating data with score-based models, 2021. URL https://arxiv.org/abs/2105.14080. 4, 7

[27] Tero Karras, Samuli Laine, and Timo Aila. A style-based generator architecture for generative adversarial networks, 2018. URL https://arxiv.org/abs/1812.04948. 4

[28] Tero Karras, Samuli Laine, and Timo Aila. A style-based generator architecture for generative adversarial networks, 2019. 8

[29] Diederik P Kingma and Jimmy Ba. Adam: A method for stochastic optimization. *arXiv preprint arXiv:1412.6980*, 2014. 13

[30] Diederik P Kingma and Max Welling. Auto-encoding variational bayes, 2013. 2, 4

[31] Durk P Kingma and Prafulla Dhariwal. Glow: Generative flow with invertible 1x1 convolutions. *Advances in neural information processing systems*, 31, 2018. 4

[32] Doyup Lee, Chiheon Kim, Saehoon Kim, Minsu Cho, and Wook-Shin Han. Autoregressive image generation using residual quantization, 2022. 5, 6, 7

[33] Jen-Yu Liu, Yu-Hua Chen, Yin-Cheng Yeh, and Yi-Hsuan Yang. Unconditional audio generation with generative adversarial networks and cycle regularization, 2020. 4

[34] Pamela Mishkin, Lama Ahmad, Miles Brundage, Gretchen Krueger, and Girish Sastry. Dall·e 2 preview - risks and limitations. 2022. URL `[https://github.com/openai/dalle-2-preview/blob/main/system-card.md](https://github.com/openai/dalle-2-preview/blob/main/system-card.md)`. 7

[35] Muhammad Ferjad Naeem, Seong Joon Oh, Youngjung Uh, Yunjey Choi, and Jaejun Yoo. Reliable fidelity and diversity metrics for generative models. 2020. 13, 17

[36] Piotr Nawrot, Szymon Tworkowski, Michał Tyrolski, Łukasz Kaiser, Yuhuai Wu, Christian Szegedy, and Henryk Michalewski. Hierarchical transformers are more efficient language models, 2021. 2, 3, 7, 9, 10

[37] Niki Parmar, Ashish Vaswani, Jakob Uszkoreit, Łukasz Kaiser, Noam Shazeer, Alexander Ku, and Dustin Tran. Image transformer, 2018. 2, 4, 17

[38] Razvan Pascanu, Tomas Mikolov, and Yoshua Bengio. On the difficulty of training recurrent neural networks, 2012. 4

[39] Adam Paszke, Sam Gross, Francisco Massa, Adam Lerer, James Bradbury, Gregory Chanan, Trevor Killeen, Zeming Lin, Natalia Gimelshein, Luca Antiga, Alban Desmaison, Andreas Kopf, Edward Yang, Zachary DeVito, Martin Raison, Alykhan Tejani, Sasank Chilamkurthy, Benoit Steiner, Lu Fang, Junjie Bai, and Soumith Chintala. Pytorch: An imperative style, high-performance deep learning library. In H. Wallach, H. Larochelle, A. Beygelzimer, F. d'Alché-Buc, E. Fox, and R. Garnett (eds.), *Advances in Neural Information Processing Systems 32*, pp. 8024–8035. Curran Associates, Inc., 2019. URL `http://papers.neurips.cc/paper/9015-pytorch-an-imperative-style-high-performance-deep-learning-library.pdf`. 13

[40] Aditya Ramesh, Mikhail Pavlov, Gabriel Goh, Scott Gray, Chelsea Voss, Alec Radford, Mark Chen, and Ilya Sutskever. Zero-shot text-to-image generation, 2021. 2, 7, 10

[41] Ali Razavi, Aaron van den Oord, and Oriol Vinyals. Generating diverse high-fidelity images with vq-vae-2, 2019. 2, 5, 7, 8

[42] Robin Rombach, Andreas Blattmann, Dominik Lorenz, Patrick Esser, and Björn Ommer. High-resolution image synthesis with latent diffusion models, 2021. 7

[43] Olga Russakovsky, Jia Deng, Hao Su, Jonathan Krause, Sanjeev Satheesh, Sean Ma, Zhiheng Huang, Andrej Karpathy, Aditya Khosla, Michael Bernstein, Alexander C. Berg, and Li Fei-Fei. Imagenet large scale visual recognition challenge, 2015. 9

[44] Nikolay Savinov, Junyoung Chung, Mikolaj Binkowski, Erich Elsen, and Aaron van den Oord. Step-unrolled denoising autoencoders for text generation, 2022. 2, 3, 6, 10, 12, 15

[45] Karen Simonyan and Andrew Zisserman. Very deep convolutional networks for large-scale image recognition, 2014. URL `https://arxiv.org/abs/1409.1556`. 10

[46] Yang Song and Stefano Ermon. Generative modeling by estimating gradients of the data distribution, 2019. 2, 4, 7

[47] Yang Song, Jascha Sohl-Dickstein, Diederik P. Kingma, Abhishek Kumar, Stefano Ermon, and Ben Poole. Score-based generative modeling through stochastic differential equations, 2020. 2, 4, 7

[48] Yang Song, Conor Durkan, Iain Murray, and Stefano Ermon. Maximum likelihood training of score-based diffusion models, 2021. 2, 4, 7

[49] Jianlin Su, Yu Lu, Shengfeng Pan, Bo Wen, and Yunfeng Liu. Roformer: Enhanced transformer with rotary position embedding, 2021. 2, 10

[50] Arash Vahdat and Jan Kautz. Nvae: A deep hierarchical variational autoencoder, 2020. URL `https://arxiv.org/abs/2007.03898`. 4, 7

[51] Arash Vahdat, Karsten Kreis, and Jan Kautz. Score-based generative modeling in latent space, 2021. 2, 4, 7

[52] Aaron van den Oord, Nal Kalchbrenner, and Koray Kavukcuoglu. Pixel recurrent neural networks, 2016. 4

[53] Aaron van den Oord, Nal Kalchbrenner, Oriol Vinyals, Lasse Espeholt, Alex Graves, and Koray Kavukcuoglu. Conditional image generation with pixelcnn decoders, 2016. 4

[54] Aaron van den Oord, Oriol Vinyals, and Koray Kavukcuoglu. Neural discrete representation learning, 2017. 2, 5, 6, 10

[55] Aaron van den Oord, Oriol Vinyals, and Koray Kavukcuoglu. Neural discrete representation learning, 2018. 8

[56] Ashish Vaswani, Noam Shazeer, Niki Parmar, Jakob Uszkoreit, Llion Jones, Aidan N. Gomez, Lukasz Kaiser, and Illia Polosukhin. Attention is all you need, 2017. 2, 4, 7

[57] Alex Wang and Kyunghyun Cho. Bert has a mouth, and it must speak: Bert as a markov random field language model, 2019. 6

[58] Zhisheng Xiao, Karsten Kreis, and Arash Vahdat. Tackling the generative learning trilemma with denoising diffusion gans, 2021. 1, 2, 7

[59] Yunyang Xiong, Zhanpeng Zeng, Rudrasis Chakraborty, Mingxing Tan, Glenn Fung, Yin Li, and Vikas Singh. Nyströmformer: A nystöm-based algorithm for approximating self-attention. In *Proceedings of the... AAAI Conference on Artificial Intelligence. AAAI Conference on Artificial Intelligence*, volume 35, pp. 14138. NIH Public Access, 2021. 7

[60] Jiahui Yu, Xin Li, Jing Yu Koh, Han Zhang, Ruoming Pang, James Qin, Alexander Ku, Yuanzhong Xu, Jason Baldridge, and Yonghui Wu. Vector-quantized image modeling with improved vqgan, 2021. 5, 6, 7

[61] Neil Zeghidour, Alejandro Luebs, Ahmed Omran, Jan Skoglund, and Marco Tagliasacchi. Soundstream: An end-to-end neural audio codec, 2021. 5, 6, 7

[62] Jun-Yan Zhu, Taesung Park, Phillip Isola, and Alexei A. Efros. Unpaired image-to-image translation using cycle-consistent adversarial networks, 2017. URL `https://arxiv.org/abs/1703.10593`. 4